Upper-Tropospheric Water Vapor from *UARS* MLS

W. G. Read,* J. W. Waters,* D. A. Flower,* L. Froidevaux,* R. F. Jarnot,* D. L. Hartmann,+ R. S. Harwood,# R. B. Rood@

Abstract

Initial results of upper-tropospheric water vapor obtained from the Microwave Limb Sounder (MLS) on the *Upper Atmosphere Research Satellite (UARS)* are presented. MLS is less affected by clouds than infrared or visible techniques, and the *UARS* orbit provides daily humidity monitoring for approximately two-thirds of the earth. Best results are currently obtained when water vapor abundances are approximately 100–300 ppmv, corresponding to approximately 12-km height in the Tropics and 7 km at high latitudes. The observed latitude variation of water vapor at 215 hPa is in good agreement with the U.K. Universities's Global Atmospheric Modelling Project model. The ability to observe synoptic-scale features associated with tropopause height variations is clearly illustrated by comparison with the National Aeronautics and Space Administration Goddard Space Flight Center assimilation model. Humidity detrainment streams extending from tropical convective regions are also observed.

1. Introduction

The global climate system is at the forefront of environmental concerns. Anthropogenic increases of greenhouse gases such as carbon dioxide could lead to enhancement of net downward radiative flux from the upper troposphere and a warmer climate. Water vapor is the most important greenhouse gas (e.g., Manabe and Wetherald 1967; Houghton et al. 1990; Jones and Mitchell 1991), and the anticipated climate change arising from any increase in the anthropogenic greenhouse gases critically depends on the water vapor response to the additional radiational forcing. Assuming that the relative humidity remains unchanged, water vapor will amplify the climate response to changes in greenhouse gas concentrations, or to any other climate forcing. The water vapor content increases exponentially with increasing temperature for a constant relative humidity. The additional water can trap more radiation and cause further heating until a new equilibrium is established (Manabe and Wetherald 1967; Betts and Ridgeway 1989). The positive feedback role of water vapor has been observed under clear-sky conditions (Raval and Ramanathan 1989; Rind et al. 1991). Water vapor and cloud abundances are highly coupled, and cloud feedback varies considerably among current general circulation models (Cess et al. 1990). Although the climate sensitivity feedback associated with water vapor is generally believed to be strongly positive, it is possible that the combined effects of clouds, precipitation, dynamics, and water vapor may act as a net negative feedback system. Lindzen (1990) argues that increased surface temperature would increase convection, which would dry the upper troposphere through subsidence. Based on cirrus cloud observations during an El Niño event, Ramanathan and Collins (1991) hypothesize that a runaway water vapor greenhouse effect over the warm oceans is checked by a negative feedback from increased reflectivity of upper-tropospheric cirrus anvils formed from condensed moist air.

Evaluation of the relative importance of these effects has been hindered by a lack of upper-tropospheric humidity (UTH) data. Understanding the climate system requires global-scale modeling, and global water vapor measurements are needed for validating general circulation model performance. The only practical method of obtaining continuous global data is through satellite observations. Significant progress is being made to acquire this information. High horizontal and temporal resolution is now available using multichannel infrared imagers aboard geostationary satellites, which includes the U.S. Geostationary Operational Environmental Satellite (Soden and Bretherton 1993; Udelhofen and Hartmann 1994) and the European Geosynchronous Meteorology Satellite (METEOSAT) (Schmetz and Turpeinen 1988) platforms. Multichannel high-resolution infrared imagers currently fly on U.S. National Oceanic and Atmospheric Administration polar-orbiting satellites that allow full global coverage with one instrument but with poorer temporal resolution. The infrared instru-

*Jet Propulsion Laboratory, California Institute of Technology, Pasadena, California.
+University of Washington, Seattle, Washington.
#University of Edinburgh, Edinburgh, United Kingdom.
@NASA/Goddard Space Flight Center, Greenbelt, Maryland.
Corresponding author address: Dr. William G. Read, Jet Propulsion Laboratory, California Institute of Technology, Mail Stop 183-701, 4800 Oak Grove Dr., Pasadena, CA 91109-8099.
In final form 15 May 1995.

ments measure radiation emitted from the 6.3-μm water band using radiometers of varying bandwidths. They all share a common feature of having limited vertical resolution, nominally a 300-hPa-thick layer centered at 300-hPa altitude, and must deal with cloud contamination. This is usually done by separating the cloud contribution as measured by a "window" or vapor-insensitive channel and estimating the clear-sky component of the water vapor channel with the N* technique (McMillin and Dean 1982) or a method by Soden and Bretherton (1993), which will work in up to 75% cloud cover. The Stratospheric Aerosol and Gas Experiment II (SAGE II) makes water vapor measurements with ~1-km vertical resolution from the stratosphere to the ground or to the cloud tops (Rind et al. 1993). SAGE II uses solar occultation, which limits its measurements to about 30 per day, with approximately one month required to cover 70°S to 70°N (Cunnold et al. 1989).

The Microwave Limb Sounder (MLS) on the *Upper Atmosphere Research Satellite (UARS)*, which has been in operation since late September 1991, gives a new capability for global UTH observations. Although not designed for this measurement, *UARS* MLS is sensitive to UTH when the field of view (FOV) of its ClO spectral band is scanned down through the troposphere, which happens once per minute on each limb scan. Important features of the MLS measurement technique for UTH are its ability to observe through cirrus and to determine vertical structure with more than 1300 profiles per day obtained from *UARS*. The vertical resolution is limited by the instrument FOV, which has a 3.0-km half-power gain width, and the best sensitivity to water vapor occurs in a vertical band where the abundance is ~150 ppmv, corresponding to ~12-km height at low latitudes and ~7 km at high latitudes. This paper describes some initial results obtained using a preliminary algorithm for extracting UTH from the MLS measurements.

2. Measurement technique

The MLS is a self-calibrating vertically scanned limb-sounding instrument that measures thermal emission in the millimeter-wavelength spectral region (Barath et al. 1993). *UARS* is in a circular 57° orbit, 585-km altitude, and MLS views the atmospheric limb in a direction perpendicular to the orbit path. There are 15 orbits per day, and MLS makes a limb scan every 4.1° of orbit arc. Geophysical profiles are extracted from measurements made during each limb scan, which covers tangent altitudes from the surface to 90 km. Calibration is performed on each limb scan. The orbital precession causes the measurement track longitude to move 5°, or 20 min earlier in local time over a 24-h period. *UARS* makes a 180° yaw maneuver approximately every 36 days, when MLS latitudinal coverage changes between 80°S–34°N and 34°S–80°N.

The MLS spectral band, which gives ClO (e.g., Waters et al. 1993), measures thermal radiation near 205-GHz frequency (wavelength ~1.5 mm), which is in a region free of any strong interfering lines in the stratospheric spectrum. When the FOV of this band is scanned down through the troposphere, the dominant contribution to its measured signal is thermal emission from water vapor. Water vapor can, in principle, be deduced from this measured signal over the vertical range between where its signals are sufficiently strong to be distinguished from other effects and where its signals become so strong that they are optically thick, and the measurements are mainly sensitive to atmospheric temperature. This range corresponds to water vapor abundances between approximately 100 and 300 ppmv. If the temperature profile is well known, the optically thick signal is a measure of relative humidity, which is the principle used by the UTH channel on infrared sensors (e.g., Soden and Bretherton 1993). This can extend the MLS measurement capability lower into the troposphere but is not considered here.

Altitude (pressure) registration of the measurements is obtained from observations of O_2 emission in the stratosphere (Waters 1993) extrapolated downward using hydrostatic equilibrium with temperatures from the operational analyses of the National Centers for Environmental Prediction (NCEP) (formerly the National Meteorological Center) and measured changes in the FOV pointing. Pointing, temperature, and *UARS* platform attitude uncertainties correspond to 400 m at 10–12 km (Fishbein et al. 1995). Figure 1 illustrates the concept for the simple retrieval scheme used for the initial results reported here. The radiance profile in the left panel is from a single limb scan near the Tropics and shows the radiance increasing with decreasing altitude, corresponding to increasing atmospheric emission, which is described by an "absorption coefficient." The measurements have been vertically interpolated onto an equal-spaced $\Delta\log_{10}$ pressure grid of 1/6 or approximately 2.5-km steps (the standard grid for *UARS* data). The plot also shows the corresponding atmospheric temperature profile from NCEP. Good sensitivity to atmospheric absorption occurs before the radiance saturates, which is above 9 km for this measurement. The instrumental noise on each 2-s integration, for the channel used here, is < 0.1 K equivalent brightness temperature, which gives a signal-to-noise ratio of greater than 1000:1 at the altitudes having best sensitivity. The radiance curve I_t in the left panel is modeled with the

differential temperature radiative transfer equation (W. G. Read, Z. Shippony, and J. W. Waters 1995, unpublished manuscript)

$$I_t = \sum_{j=t+1}^{N} T_j^R \prod_{k=j}^{N} \delta_{kt} - \left(\prod_{k=t}^{N} \delta_{kt}\right) \times \left(\sum_{j=t+1}^{N} T_j^L \prod_{k=t}^{j-1} \delta_{kt}\right). \quad (1)$$

This equation is applied to an $N-1$ layered atmosphere where each layer is separated by a surface with indices running from 1 (the earth surface) to N (top of the $N-1$ layer and nonabsorbing space). The N levels correspond to the radiance measurement heights, which in this case have been interpolated from the actual measurements onto the standard *UARS* output grid as described above. Subscript t denotes the limb tangent surface, and i, j, and k indicate the surfaces used in the products and sums. Here $T_i^L = T_i^R = (T_{i-1} - T_{i+1})/2$ except when $i = N$, where $T_N^R = (T_{N-1} + T_N)/2$ and $T_N^L = T_N^R - T^s$: T_i and T^s are the atmospheric brightness temperature (i.e., Planck radiation energy divided by the Boltzmann constant) at the ith surface and cosmic background, respectively. The term δ_{it} is the layer transmission given by

$$\delta_{it} = \exp(-\alpha_i \Delta s_{it}), \quad (2)$$

where α_i is the average absorption coefficient between surfaces i and $i+1$, and Δs_{it} is the pathlength between surfaces i and $i+1$ having a path geometry passing tangentially through surface t ($\delta_{Nt} \equiv 1$ and $\alpha_N \equiv 0$). Refraction is ignored here. Equation (1) can be recast into a recursion equation that yields a vertical profile of layer absorption coefficient using

$$\alpha_t = \ln \frac{\left(\dfrac{\prod_{i=t+1}^{N} \delta_{it} \sum_{i=t+1}^{N} T_i^L \prod_{j=t+1}^{i-1} \delta_{jt}}{\sum_{i=t+1}^{N} T_i^R \prod_{j=i}^{N} \delta_{jt} - I_t}\right)}{(2\Delta s_{tt})}. \quad (3)$$

The center panel of Fig. 1 shows the result of applying Eq. (3) to the radiance profile using the $\Delta \log_{10} P = 1/6$ thick layers for each step. The FOV smearing is ignored in the simple procedure used here, which has the effect of degrading resolution and introducing biases. Also shown in the center panel is empirical dry atmosphere continuum emission (determined by us), which dominates the signal above the tropopause. This continuum emission is present in all MLS stratospheric radiances and is nearly invariant with season and latitude (including the cold dry southern vortex), indicating that it is not caused by water vapor, clouds, or aerosols. It is probably caused by collision-induced absorption (CIA) among nitrogen and oxygen molecules. Nitrogen CIA has been measured at other frequencies (Dagg et al. 1985; Borysow and Frommhold 1986), and an empirical function can be determined that fits the data between 0 and 450 GHz and 126 and 333 K to better than 10%. Unfortunately, this accounts for only 62% (0.79^2 N_2 abundance) of the total continuum. The remaining 38% must be estimated as follows. If nitrogen CIA with oxygen is identical to itself, then the empirical function can be used for 79% of the absorption. The remaining 21% comes from O_2 CIA and dipole absorption, where absorption by any of the trace atmospheric gases is omitted. (This is likely to add less than 5% to the dry continuum in the troposphere.) The O_2 contribution can be estimated by extrapolating the Liebe et al. (1992) Millimeter-wave Propagation Model (MPM) O_2 absorption model, which is derived from line-by-line absorption measurements. Combining the N_2 and O_2 absorption coefficient models produces a func-

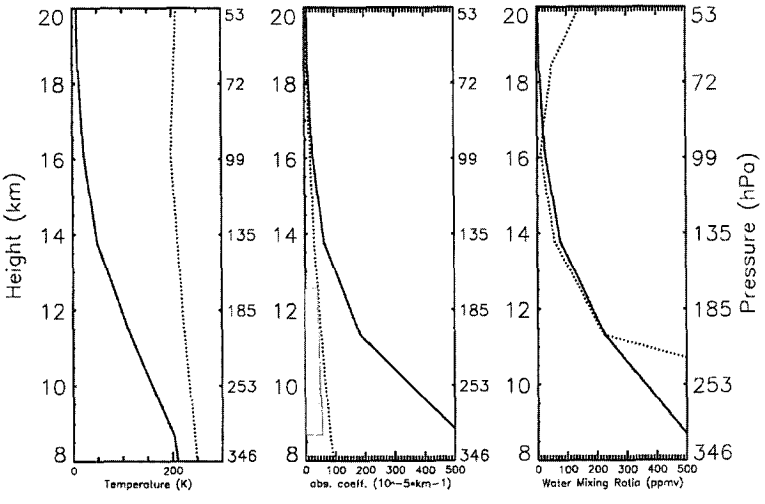

FIG. 1. Illustration of upper-tropospheric water vapor retrieval scheme used here. The left panel shows measured radiances (solid line) and NCEP temperatures (dotted line) interpolated onto an equally spaced $\log_{10}$-pressure altitude grid. The center panel shows conversion to absorption coefficient (solid line). The contribution due to cirrus can have values inside the shaded region whose rightmost extent is indicative of a 120-km horizontally thick and 0.1 g m^{-3} ice content cirrus. The dotted line is the absorption coefficient from the empirically derived collision-induced dry air absorption. The right panel is the retrieved water vapor profile (solid line) after subtracting the dry air continuum but ignoring any cirrus contributions. A 100% ice-relative humidity curve (dotted line) is shown for comparison. This example is for a tropical measurement having high water content.

tion that differs from the experimental continuum derived from stratospheric MLS measurements by 25% in the upper troposphere. Considering the degree of uncertainty associated with these two continuum functions, this is a reasonable agreement and serves to validate the source of the unknown emission. The dry air continuum is subtracted from the measured absorption coefficient, and the difference is converted to water vapor concentration using Liebe's (1989) MPM. The result is shown in the right panel of Fig. 1. It should be noted that when the atmosphere has less than 100 ppmv humidity at 215 hPa, more than 50% of the signal comes from the dry air continuum emission. Based on comparing the two functions described above, there probably exists at least a 25% systematic error in the function being subtracted from the total absorption coefficient in the middle panel. At 215 hPa, this is roughly 25 ppmv humidity, which is a large relative error when the concentrations are low. Fortunately, despite uncertainties in the current knowledge of the continuum, the functional form is simple and well established experimentally, and through a careful validation exercise, an effective function can be accurately established from the measurements that will improve the accuracy when the values are low. High retrieved water vapor values (>300 ppmv) can be erroneous because of limitations in the retrieval technique. High values cause both the numerator and the denominator in Eq. (3) to trend toward zero, which makes the inversion very sensitive to any error such as neglecting FOV effects, atmospheric temperature, and computational numerics. In the future this will be circumvented with a retrieval technique designed for saturated radiances.

Figure 1 also shows the calculated effects of ice on MLS 205-GHz measurements based on the theory given by Gunn and East (1954) and a dielectric model from Liebe et al. (1989). The MLS UTH measurements are at altitudes that can be populated by cirrus anvils from deep convective towers. Measurements of ice crystals in cirrus anvils have revealed ice mass densities up to 0.1 g m^{-3} and particle sizes of 20–40 μm at temperatures < 220 K over spatial scales of 120 km (Knollenberg et al. 1993). This amount of ice could contribute ~20% to the total absorption coefficient at 12 km, as shown in Fig. 1. In practice it will usually be less, because these are maximum values and not likely to be realized over the synoptic scales on which MLS makes measurements. The relative strengths of emission at 205 GHz due to water in ice:vapor:liquid are 1:2:100 for equal mass densities; lower-altitude clouds containing liquid water > 0.1 g m^{-3} (typical for a light cumulus cloud) will mask the vapor signal. The profile shown in Fig. 1 is characteristic of a wet atmosphere (as compared to other MLS measurements) and is likely in the presence of convective cumulative towers. The shaded bar indicates the potential magnitude of cloud effects and the vertical extent may be greater than shown. No contribution from clouds has been subtracted from the total absorption in the water estimate shown in the right panel. The supersaturation shown in the right panel could be due to cloud emission, continuum errors, and other errors. Again, note that the measurement is mostly dry continuum above 146 hPa. Higher-altitude polar stratospheric clouds and nonconvective cirrus clouds are more than 30 times less dense [typically < 0.003 g m^{-3} at T < –40°C (Heymsfield and Platt 1984)] than tropical convective cirrus anvils, and their effects on MLS water vapor measurements are *negligible*.

A test of the relative insensitivity to ice clouds is provided by MLS observations on 8 February 1993 through Tropical Cyclone Oliver over the Coral Sea. The particle microphysics in Oliver were characterized by aircraft experiments and reported by Pueschel et al. (1995), who find very high ice densities in the range of 0.4–1.0 g m^{-3}, and having a bimodal particle size distribution with peaks of 0.04 and 0.4 mm diameter at 10.7 km. They also found that particle concentrations increased with altitude up to 10.7 km. Based on Knollenberg et al. (1993), these conditions are up to 10 times more severe than found in isolated convective systems. Shown in Fig. 2 are three MLS measurement tracks at 215 hPa, where the track indicated by stars goes through the cyclone and the other two tracks are adjacent and avoid it. The latitudinal extent of the storm shown in the shading is based on the image in Fig. 1 of Pueschel et al. (1995). The MLS measurement track over Oliver detects humidification (relative to the two adjacent tracks) in a reasonable 80%–90% range, showing that the effect of condensed water in this cyclone is not readily

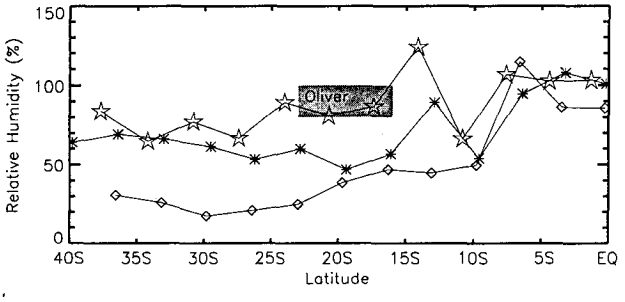

FIG. 2. Retrieved relative humidity along three adjacent MLS measurement tracks within 0°–40°S latitude and 130°–170°E longitude at 215 hPa on 8 February 1993. The Oliver cyclone location is shaded, and the track denoted by stars goes through it. The track depicted with diamonds is to the east over ocean, and asterisks depict the track to the west and mostly along the Australian east coast.

apparent in the vapor measurement. An unrealistically high value of 130% was measured immediately north of the storm and is not yet understood. Note that retrieved values on all three MLS measurement tracks increase to near 100% relative humidity in the Tropics, which might be expected because these tracks pass over the typically moist Indonesian region.

3. Some initial results

The initial MLS water vapor results shown here are for a 100-hPa-thick layer centered at 215 hPa and assume no contribution from ice. It is difficult to validate the retrieved water vapor distribution against other measurements because of the lack of suitable datasets. Therefore, we will evaluate the phenomenology of the datasets by comparison with model results and related observations that are expected to be closely related to UTH. Figure 3 shows simulated distributions from the UGAMP (U.K. Universities's Global Atmospheric Modelling Project) model (e.g., Gray et al. 1993). This is a spectral 19-level (hybrid sigma and p) model extending from the surface to 10 hPa, derived from the forecasting model of the European Centre for Medium-Range Weather Forecasts. The runs used here were initialized with July conditions, and the data for Fig. 3 were extracted 12 and 18 months into the run. These experiments used triangular-21 truncation, the Kuo convective scheme, and specified sea surface temperatures corresponding to 1987 observations. The model calculation is water vapor at 215 hPa; however, the vertical resolution of the model (~0.11 in log p) effectively smooths the vertical profile, and although the nature of the smoothing will differ between the MLS and the UGAMP, it does not affect the conclusions being drawn here. Figure 3 shows individual measurements and the zonal mean for a pair of days taken before and after a *UARS* yaw maneuver in both January and July 1992. The latitudinal distribution of the MLS measurements are consistent with the simulation. Maximum values occur in the subtropics of the summer hemisphere. The peak zonal value observed by MLS shows less displacement from the equator than the UGAMP model. The largest differences occur at high latitudes, where MLS values can be artificially high due to FOV effects, which are not accounted for in the preliminary retrieval algorithms used here. Nonetheless, the comparison shows that UTH from MLS has the basic structure expected from climate model simulations.

An interhemispheric asymmetry in UTH has been observed from aircraft in situ measurements by Kelly et al. (1991). This interhemispheric asymmetry is considered a robust feature and has been used to try to understand the relationship between water vapor and general circulation. Kelly et al. (1991) found the wintertime UTH poleward of 40° to be 50%, or 10 ppmv, drier in the Southern Hemisphere than in the Northern Hemisphere. The MLS zonal average poleward of 40° also shows a ~10 ppmv drier South-

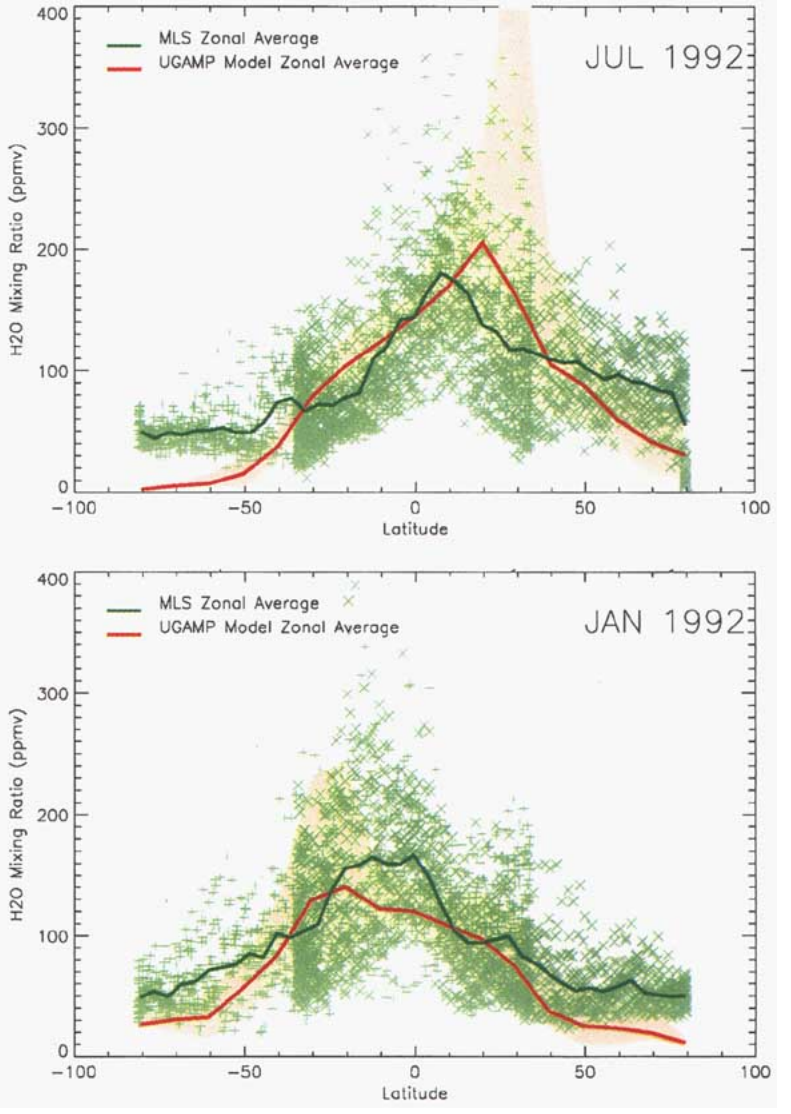

FIG. 3. January and July H_2O versus latitude. Green × and + are individual MLS measurements from two days. Red shaded area indicates the range of values predicted by the U.K. UGAMP model.

ern Hemisphere. The larger absolute values in the MLS are a bias caused by neglecting FOV effects and averaging through the 2.5–3.0-km-thick layer. A definitive MLS statement regarding the wintertime asymmetry requires an improved retrieval algorithm currently being developed. Since the aircraft results were based on cloud-free data below the tropopause, coincident data on clouds and tropopause altitude would be needed.

Upper-tropospheric water vapor measurements in the tropical west Pacific were made during the National Aeronautics and Space Administration (NASA) Pacific Exploratory Mission West-A (PEMWA) during September–October 1991 using a Lyman-α instrument on a DC-8 aircraft (Kelly et al. 1993). Near-coincident MLS measurements have been compared with the PEMWA measurements and reasonably good agreement is obtained (Newell et al. 1995a). The MLS measurements also show a distribution of UTH that is consistent with the Walker circulation and its seasonal variation (Newell et al. 1995b).

Comparison of UTH from MLS and Goddard Earth Observing System Version 1 (GEOS-1) data assimilation system (Schubert et al. 1993, 1995) relates the MLS measurements to radiosonde observations. It also offers a mechanism to assess the synoptic variability of the observations. The GEOS-1 assimilation extends from the ground to 10 hPa, but moisture data from radiosondes is included only up to 300 hPa. As the assimilating model proceeds, moisture information is propagated to altitudes higher than 300 hPa. A demonstration of the MLS ability to track synoptic-scale UTH features is shown in Fig. 4 through comparison with GEOS-1. The maps are for 14 March 1993, when the U.S. east coast was experiencing a severe blizzard. The GEOS-1 humidity map was produced from data sampled according to the MLS orbit. The main features associated with the storm are in good agreement between the MLS measurements and the assimilation model. Also shown in Fig. 4 is the tropopause pressure from GEOS-1. The clash between the tropospheric and stratospheric air along the east coast of the United States, as shown in both GEOS-1 fields, is clearly indicated in the MLS map by a sharp water vapor gradient. Other features also correlate well between the tropopause height and MLS maps, but not so well with the GSFC humidity map. Notably, an arm of high-tropopause pressure associated with dry air extending northwest from Hawaii and an unusually low pressure tropopause and a wet region occurring north of the Chukchi Sea (70°N, 170°W) are present. A

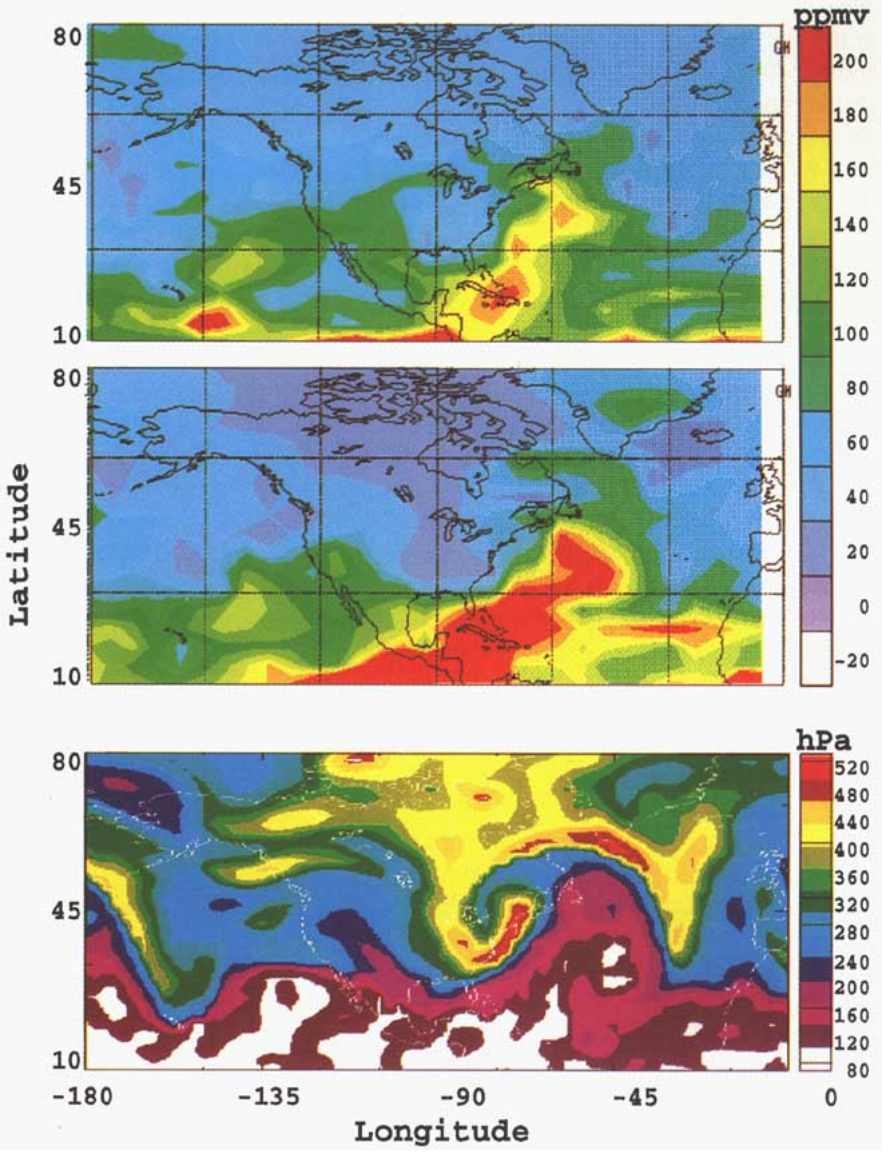

FIG. 4. Top panel shows MLS 215-hPa water vapor on 14 March 1993 when the eastern coast of the United States was experiencing a severe blizzard. The center panel shows a humidity map from the Goddard Space Flight Center (GSFC) assimilation model that has been sampled similar to MLS. The bottom panel shows the tropopause pressure for the same day from the GSFC assimilation model.

significant difference is the existence of quite moist air in the assimilation result as far north as Greenland where the MLS indicates dry air. An interesting moist feature at 25°N, 140°W correlates very well between MLS and GEOS-1 and does not have an associated feature in the tropopause pressure.

The tropopause pressure map shows whether air at 215 hPa is in the stratosphere and hence should be dry, or is in the troposphere and should be moist. The East Coast blizzard is a very large event that occurred over a region where the radiosonde network is dense and the GEOS-1 humidity map should be of high quality. This distinct synoptic event, coupled with the dense radiosonde observations, provides good validation that the MLS can detect synoptic variability. The presence of consistent features over the Pacific between the tropopause pressure maps and MLS water vapor also provides validation information. Over the Pacific, radiosonde moisture data are sparse. The tropopause pressure from the assimilation is derived from satellite temperature measurements. The MLS detects a signature in the moisture field, which is verified by the pattern of the assimilation tropopause pressure. This shows that in the absence of moisture observations being directly assimilated into GEOS-1, the moisture fields from GEOS-1 contain significant errors. This demonstrates that future assimilations using MLS can change even the qualitative representation of UTH.

Comparisons between fractional area coverage by high (above 440 hPa) and optically thick (visible optical depth greater than 9.38) clouds and the MLS upper-tropospheric water distribution are shown in Figs. 5 and 6. The cloud cover maps are the 1983–90 climatology and indicate the regions where deep convective clouds are prevalent. These are derived from the International Satellite Cloud Climatology Project C1 dataset (Rossow and Schiffer 1991; Hartmann et al. 1992). The MLS upper-tropospheric water distributions were obtained by averaging all usable data from 1991 to 1994 and represent our first attempt at a climatology of tropospheric water vapor from MLS. Although the cloud and UTH maps are for different years, the correspondence is good, as expected since convective areas occur in the same general region from year to year. The MLS maps clearly show regions where detrainment streams regularly extend from the convective (cloudy) regions. The divergence of water vapor from the tropical convective zones is important to determine because the outgoing longwave radiation, and hence the global greenhouse budget, critically depend on it.

Comparison of MLS averages with SAGE II [compare plate 1 of Rind et al. (1993), 300-mb water vapor

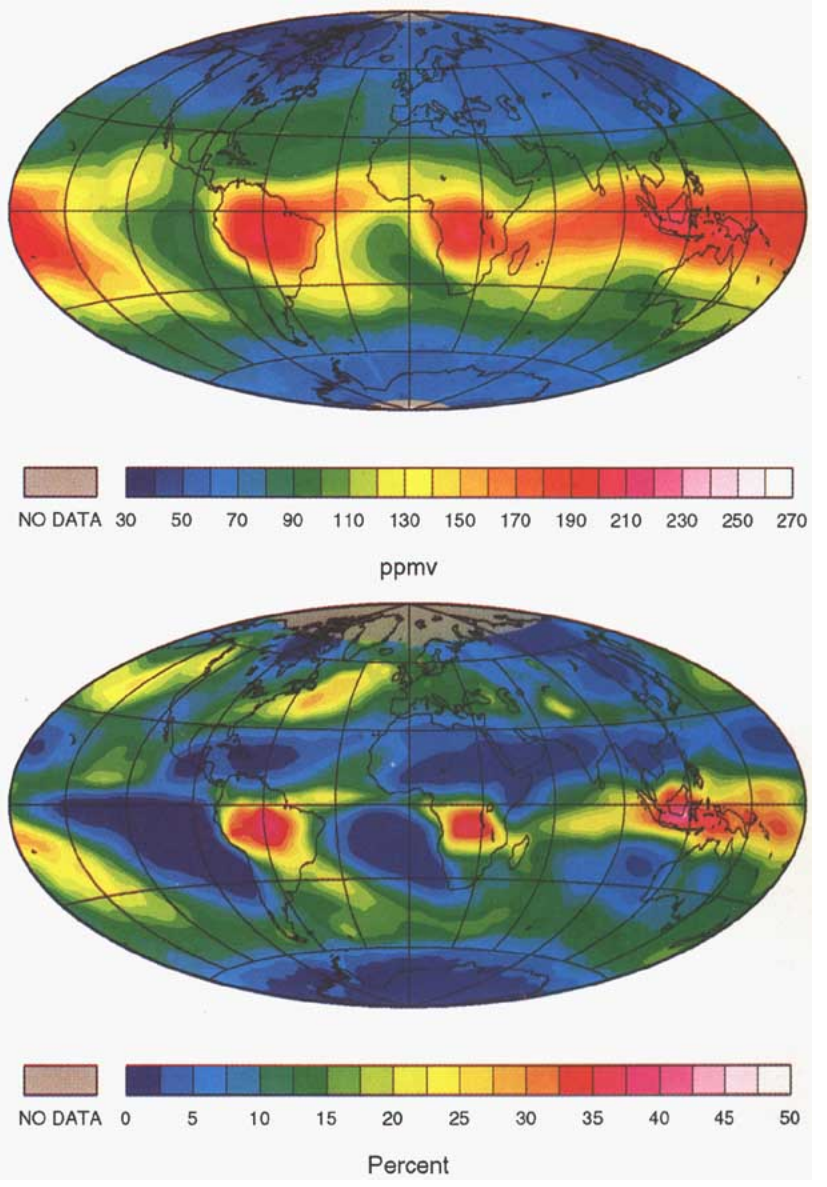

FIG. 5. Top panel shows the 215-hPa MLS water vapor climatology for December–February that uses measurements made from 1991 to 1993 binned into 4° × 4° latitude/longitude boxes. The bottom panel shows the December–February, 1983–90 ISCCP fractional high thick (altitude above 440 hPa and visible optical depth greater than 9.38) cloud cover climatology map.

with Figs. 5 and 6] show mixed results. The SAGE II climatologies are from 1-month averages using 5 yr of data sampled 30 profiles per day with no measurements in cloudy conditions. The MLS averages show moist areas originating within regions of high cloudiness and spreading outward. SAGE II climatologies have no measurements (due to perpetual cloudiness) coincident with high MLS humidity values, but with the surrounding regions showing large inhomogeneity where MLS shows uniformly moist air. For example, the SAGE II January map has no UTH measurements in Indonesia, yet the region is largely bounded by extremely dry air. Also, the MLS maps show high humidity over the equatorial continents and dryness over the Atlantic and Pacific Oceans, while SAGE II shows this in July, but SAGE II shows South America being drier than the central Pacific in January. Both SAGE II and MLS show moisture streams extending far north from the Tropics to high northern latitudes along the eastern U.S. coast and eastern Japan. The intercomparison features described here are probably caused by sampling differences between the MLS and SAGE II measurements.

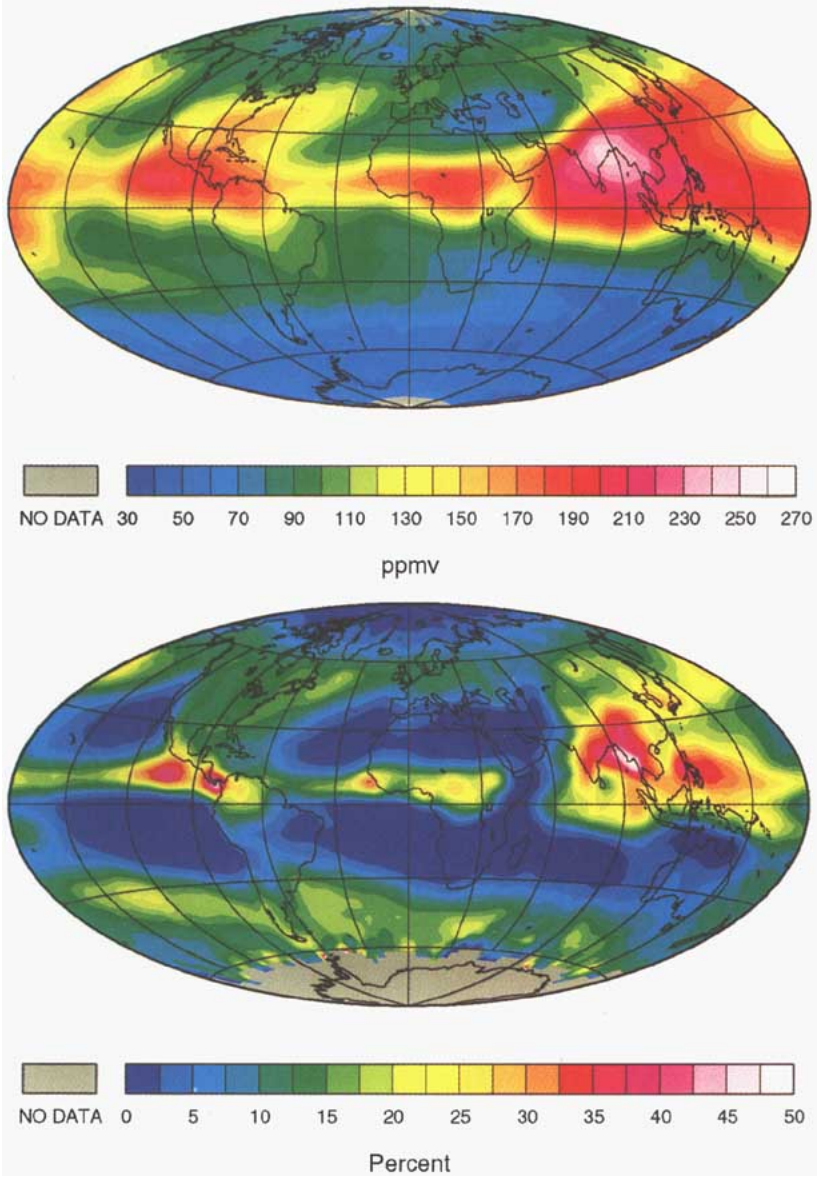

FIG. 6. Top panel shows the 215-hPa MLS water vapor climatology for June–August that uses measurements made from 1992 to 1993 binned into 4° × 4° latitude–longitude boxes. The bottom panel shows the June–August 1983–90 ISCCP fractional high thick (altitude above 440 hPa and visible optical depth greater than 9.38) cloud cover climatology map.

4. Future work

The initial results shown here indicate MLS can provide information on global upper-tropospheric water vapor. Future work will include development of a more sophisticated algorithm to provide useful quantitative values and validation of the resulting product. A next-generation MLS is now being developed for NASA's Earth Observing System. It will continue the *UARS* upper-tropospheric water measurements to provide a long-term record and will also have enhanced capability to include complete coverage of water vapor from the upper troposphere through the stratosphere. Such measurements, it is hoped, will advance our knowledge of earth's climate system and the potential for changes in it.

Acknowledgments. We thank Mark Schoeberl (*UARS* Project Scientist) for encouraging us to pursue the MLS upper-tropospheric water vapor measurement capability. The research described here, done at the Jet Propulsion Laboratory, California Institute of Technology, was under contract with the National Aeronautics and Space Administration and funded through its *UARS* Project. Support for DLH was provided by NASA Grant NAGW-2633, and NERC provided support for the U.K.UGAMP calculations by RSH. We thank Dave Ledvina from GSFC for providing the GEOS-1 figures.

References

Barath, F., and Coauthors, 1993: The *Upper Atmosphere Research Satellite* Microwave Limb Sounder instrument. *J. Geophys. Res.*, **98,** 10 751–10 762.

Betts, A. K., and W. Ridgeway, 1989: Climatic equilibrium of the atmospheric convective boundary layer over a tropical ocean. *J. Atmos. Sci.*, **46,** 2621–2641.

Borysow, A., and L. Frommhold, 1986: Collision-induced rotranslational absorption spectra of N_2–N_2 pairs for temperatures from 50 to 300 K. *Astrophys. J.*, **311,** 1043–1057.

Cess, R. D., and Coauthors, 1990: Intercomparison and interpretation of climate feedback processes in 19 atmospheric general circulation models. *J. Geophys. Res.*, **95,** 16 601–16 616.

Cunnold, D. M., W. P. Chu, R. A. Barnes, M. P. McCormick, and R. E. Veiga, 1989: Validation of SAGE II ozone measurements. *J. Geophys. Res.*, **94,** 8447–8460.

Dagg, I. R., A. Anderson, S. Yan, W. Smith, and L. A. A. Read, 1985: Collision-induced absorption in nitrogen at low temperatures. *Can. J. Phys.*, **63,** 625–631.

Fishbein, E. F., and Coauthors, 1995: Validation of *UARS* MLS temperature and pressure measurements. *J. Geophys. Res.*, in press.

Gray, L. J., M. Blackburn, M. P. Chipperfield, J. D. Haigh, D. R. Jackson, K. P. Shine, J. Thuburn, and W. Zhong, 1993: First results from a 3-dimensional middle atmosphere model. *Adv. Space Res.*, **13,** 363–372.

Gunn, K. L. S., and T. W. R. East, 1954: The microwave properties of precipitation particles. *Quart. J. Roy. Meteor. Soc.*, **80,** 522–545.

Hartmann, D. L., M. E. Ockert-Bell, and M. L. Michelson, 1992: The effect of cloud type on earth's energy balance: Global analysis. *J. Climate*, **5,** 1281–1304.

Heymsfield, A. J., and C. M. R. Platt, 1984: A parameterization of the particle size spectrum of ice clouds in terms of the ambient temperature and the ice water content. *J. Atmos. Sci.*, **41,** 846–855.

Houghton, J. T., G. J. Jenkins, and J. J. Ephraums, 1990: *Climate Change. The IPCC Scientific Assessment.* Cambridge University Press, 365 pp.

Jones, R. L., and J. F. B. Mitchell, 1991: Is water vapour understood? *Nature*, **353,** 212.

Kelly, K. K., A. F. Tuck, and T. Davies, 1991: Wintertime asymmetry of upper tropospheric water between the Northern and Southern Hemispheres. *Nature*, **353,** 244–247.

——, M. H. Proffitt, K. R. Chan, M. Loewenstein, J. R. Podolske, S. E. Strahan, J. C. Wilson, and D. Kley, 1993: Water vapor and cloud water measurements over Darwin during the STEP 1987 tropical mission. *J. Geophys. Res.*, **98,** 8713–8723.

Knollenberg, R. G., K. Kelly, and J. C. Wilson, 1993: Measurements of high number densities of ice crystals in the tops of tropical cumulonimbus. *J. Geophys. Res.*, **98,** 8639–8664.

Liebe, H. J., 1989: MPM—An atmospheric millimeter-wave propagation model. *Int. J. IR and MM Waves*, **6,** 631–650.

——, T. Manabe, and G. A. Hufford, 1989: Millimeter-wave attenuation and delay rates due to fog/cloud conditions. *IEEE Trans. Antennas Propagat.*, **37,** 1617–1623.

——, P. W. Rosenkranz, and G. A. Hufford, 1992: Atmospheric 60-GHz oxygen spectrum: New laboratory measurements and line parameters. *J. Quant. Spectrosc. Radiat. Transfer*, **48,** 629–643.

Lindzen, R. S., 1990: Some coolness concerning global warming. *Bull. Amer. Meteor. Soc.*, **71,** 288–299.

Manabe, S., and R. T. Wetherald, 1967: Thermal equilibrium of the atmosphere with a given distribution of relative humidity. *J. Atmos. Sci.*, **24,** 241–259.

McMillin, L. M., and C. Dean, 1982: Evaluation of a new operational technique for producing clear radiance. *J. Appl. Meteor.*, **21,** 1005–1014.

Newell, R. E., Y. Zhu, E. V. Browell, S. Ismail, W. G. Read, J. W. Waters, K. K. Kelly, and S. C. Liu, 1995a: Upper tropospheric water vapor and cirrus: Comparison of DC-8 observations, preliminary *UARS* MLS measurements and meteorological analysis. *J. Geophys. Res.*, in press.

——, ——, ——, W. G. Read, and J. W. Waters, 1995b: Walker circulation and tropical upper tropospheric water vapor. *J. Geophys. Res.*, in press.

Pueschel, R. F., D. A. Allen, C. Black, S. Faisant, G. V. Ferry, S. D. Howard, J. M. Livingston, J. Redemann, C. E. Sorenson, and S. Verma, 1995: Condensed water in Tropical Cyclone "Oliver," 8 February 1993. *Atmos. Res.*, **38,** 297–313.

Ramanathan, V., and W. Collins, 1991: Thermodynamic regulation of ocean warming by cirrus clouds deduced from observations of the 1987 El Niño. *Nature*, **351,** 27–32.

Raval, A., and V. Ramanathan, 1989: Observational determination of the greenhouse effect. *Nature*, **342,** 758–761.

Rind, D., E.-W. Chiou, W. Chu, J. Larsen, S. Oltmans, J. Lerner, M. P. McCormick, and L. McMaster, 1991: Positive water vapour feedback in climate models confirmed by satellite data. *Nature*, **349,** 500–503.

——, ——, ——, S. Oltmans, J. Lerner, J. Larsen, M. P. McCormick, and L. McMaster, 1993: Overview of the Stratospheric Aerosol and Gas Experiment II water vapor observations: Method, validation, and data characteristics. *J. Geophys. Res.*, **98,** 4835–4856.

Rossow, W. B., and R. A. Schiffer, 1991: ISCCP cloud data products. *Bull. Amer. Meteor. Soc.*, **72,** 2–20.

Schmetz, J., and O. M. Turpeinen, 1988: Estimation of the upper tropospheric relative humidity field from METEOSAT water vapor image data. *J. Appl. Meteor.*, **27,** 889–899.

Schubert, S. D., R. B. Rood, and J. Pfaendtner, 1993: An assimilated dataset for earth science applications. *Bull. Amer. Meteor. Soc.*, **74,** 2331–2342.

——, C.-K. Park, C.-Y. Wu, W. Higgins, Y. Kondratyeva, A. Molod, L. Takacs, M. Seablom, and R. Rood, 1995: A multiyear assimilation with the GEOS-1 system: Overview and results. NASA Tech. Memo. 104606, 207 pp.

Soden, B. J., and F. P. Bretherton, 1993: Upper tropospheric relative humidity form the GOES 6.7 μm channel: Method and climatology for July 1987. *J. Geophys. Res.*, **98,** 16 669–16 688.

Udelhofen, P. M., and D. L. Hartmann, 1994: Influence of tropical cloud systems on the relative humidity in the upper troposphere. *J. Geophys. Res.*, **100,** 7423–7440.

Waters, J. W., 1993: Microwave limb sounding. *Atmospheric Remote Sensing by Microwave Radiometry,* M. A. Janssen, Ed., John Wiley and Sons, Inc., 572 pp.

——, L. Froidevaux, W. G. Read, G. L. Manney, L. S. Elson, D. A. Flower, R. F. Jarnot, and R. S. Harwood, 1993: Stratospheric ClO and ozone from the Microwave Limb Sounder on the *Upper Atmosphere Research Satellite. Nature*, **362,** 597–602.

Wu, X., J. J. Bates, and S. S. Khalsa, 1993: A climatology of the water vapor band brightness temperatures from NOAA operational satellites. *J. Climate*, **6,** 1282–1300.